Elsevier Editorial System(tm) for Scripta Materialia

Manuscript Draft

Manuscript Number: SMM-19-510R2

Title: Probing the Subsurface Lattice Rotation Dynamics in Bronze after Sliding Wear

Article Type: Regular article

Keywords: EBSD; TEM; bronze; wear; grain re-orientation

Corresponding Author: Professor Wenjun Cai,

Corresponding Author's Institution:

First Author: Wenjun Cai

Order of Authors: Wenjun Cai; Pascal Bellon; Armand J Beaudoin

Abstract: The subsurface lattice rotation of polycrystalline and single crystal Cu-Ni-Sn bronze after pin-on-disc wear test were characterized using electron-backscattered diffraction and transmission electron microscopy. The majority of grains were sheared in the sliding direction with rotation axis around the transverse direction of the pin, exhibiting a weak shear texture. The orientation spread along the sliding direction increased with subsurface plastic strain, following a power law relationship. The grain re-orientation magnitude in the pin normal direction was found to be related to the number of active slip systems, as indicated by the Schmid Factors of the local grain orientation.

Probing the Subsurface Lattice Rotation Dynamics in Bronze after Sliding Wear

W. Cai[1,*], P. Bellon[2], and A. J. Beaudoin[3]

[1]Department of Materials Science and Engineering, Virginia Polytechnic Institute and State University, Blacksburg, Virginia 24060, United States

[2]Department of Mechanical Science and Engineering, University of Illinois at Urbana-Champaign, 1304 W. Green St, Urbana, IL 61801, USA

[3]Department of Mechanical Engineering, University of Illinois at Urbana-Champaign, 1206 W. Green St, Urbana, IL 61801, USA

*: caiw@vt.edu

Abstract

The subsurface lattice rotation of polycrystalline and single crystal Cu-Ni-Sn bronze after pin-on-disc wear test were characterized using electron-backscattered diffraction and transmission electron microscopy. The majority of grains were sheared in the sliding direction with rotation axis around the transverse direction of the pin, exhibiting a weak shear texture. The orientation spread along the sliding direction increased with subsurface plastic strain, following a power law relationship. The grain re-orientation magnitude in the pin normal direction was found to be related to the number of active slip systems, as indicated by the Schmid factors of the local grain orientation.

Keywords: EBSD; TEM; bronze; wear; grain re-orientation

Dry sliding wear of metals often leads to severe plastic deformation and the development of sharp strain gradient in the subsurface material. Such severe plastic deformation translates into extensive lattice rotation, grain subdivision, and elevated dislocation density right below the sliding surface. While extensive work in the field of tribology has focused on characterizing the microstructure and chemistry of the tribolayer [1-8], little has been done to quantify the grain level plasticity [9-13], which directly impacts the surface crystallographic texture, work hardening ability, and tribological response of the material. In this work, dry sliding wear tests were performed on face-centered cubic polycrystalline and single crystal bronze. By imposing an appropriate normal load during wear, the whole plastically deformed zone was well confined within individual grains. This method makes it possible to probe the continuous lattice rotation kinetics up to large plastic strains (~ 181%), higher than those previously reported [14-18]. The study addresses in particular of how local crystallographic orientation influences subsurface grain rotation and plastic strain development, and provides unique local-scale experimental data that could be potentially used to test and validate crystal plasticity models where shear deformation dominates, such as those in wear [19], equal channel angular pressing [20], high pressure torsion [21], and additive friction stir manufacturing [22] etc.

Self-mated dry sliding wear tests were performed using a Koehler K93500 pin-on-disc (POD) tester at room temperature in air (Fig. 1(a)). Both the pin (6 mm diameter) and the disc (105 mm diameter and 5 mm thick) were made from a spinodally-hardened single-phase face-centered cubic (fcc) bronze (Cu-15wt% Ni-8wt% Sn) with a mean grain size ≈ 150 μm, determined using line intercept method from polished samples. This particular material was chosen here due to a combination of high hardness, relatively large grain size, and homogenous microstructure within individual grains in the as-received state. The high hardness ensures that significant lattice rotation instead of grain subdivision or subgrain formation dominates during wear. The relatively large grain size of the bronze ensures that all plastic deformation could be confined to an individual grain since the size of the plastically deformed zone (PDZ) was ~ 10-15 μm (shown later in Fig.1), much smaller than the grain size. In

addition, the sizes of the grain boundary affected zones (GBAZs) were typically less than ~ 5 μm (see supplemental material Fig. S1 [23]), also much smaller than the grain size. Thus local grain reorientation could be investigated from areas far away from the GBAZs to minimize grain boundary effects. Finally, the homogenous microstructure within individual grains, i.e. the absence of lattice curvature or local misorientation variations, ensures that lattice rotation due to wear can be unambiguously tracked from an initial orientation in the undeformed state. In addition to the polycrystalline pins, three single crystal bronze pins were also studied. Using the same wear condition and the same type of material (except grain size), it is expected that the subsurface strain profile in the single crystal would be similar to that of the polycrystalline material (since areas close to grain boundaries were avoided in the polycrystalline material). A normal load of 0.5 kgf (or 0.17 MPa normal pressure) and 0.05 m/s sliding speed were applied for 4 hours for the POD tests. The selection of this low load ensures that grain reorientation dominates during wear, instead of grain subdivision or subgrain formation, which were observed under a higher load of 10 kgf [24]. The duration of the test was chosen to ensure steady-state was reached. Steady state wear rate and friction coefficient of the pin were measured to be 1.26 $\times 10^{-6}$ mm^3/mm and 0.74, respectively. Microstructural characterization and orientation mapping were performed on polished sample cross-sections after wear test using a JEOL 7000F SEM equipped with a HKL Technology electron-backscattered diffraction (EBSD) system at step size of 10 to 50 nm. Transmission electron microscopy (TEM, JEOL 2010F) analysis were performed on cross-section samples prepared by the standard lift-out technique using a focused ion beam (FIB, FEI) microscope.

Directly underneath the sliding surface, a PDZ of about 10 – 15 μm was observed, as shown by EBSD (Fig. 1(b)) and TEM (Fig.1 (e)) analyses. Fig. 1(e) shows the bright-field TEM images of the cross-section of the polycrystalline bronze pin after wear, with representative subsurface microstructure around 1.5, 5, and 13 μm below the surface from a single grain. It can be seen that subsurface dislocation densities increases towards the surface, indicating the presence of a sharp strain gradient within an individual grain. Right below the surface, significant grain subdivision was not

observed, unlike those under higher loads (e.g. 10 kgf as reported earlier [1, 24]). Furthermore, EBSD and TEM study shows that under the current wear condition, twining is not often observed, so that the dominating deformation mechanism can be considered as dislocation slip. Subsurface lattice rotation within the PDZ is characterized by a continuous color change in the EBSD map, as shown in Fig. 1(b). The deformation is fairly uniform in the sliding direction (SD), where no grain splitting was observed except those very close to the grain boundaries (GBs). In this work, analysis was done focusing on areas far away from these GBAZs. Subsurface plastic deformation was quantified by the strain profile in Fig 1(c), measured using the marker displacement method using grain boundaries as markers [25]. Such measurements were performed on five general GBs and five twin boundaries (more details provided in [23]). The equivalent von Mises strain (ε_{vM}) increases with decreasing depth (d) from the surface, following an exponential decay [26]

$$\varepsilon_{vM} = \varepsilon_0 \exp(-d/D), \quad (1)$$

where the decay length D = 6.14 ± 1.24 μm. The maximum strain ε_0, reached at the wear surface, was 181 ± 52% (or 313% shear strain). The maximum strain rate at the surface was estimated to be ≈ 1×10^{-3} s^{-1}, assuming wear reaches steady-state condition [27]. Fig. 1(d) shows the {111} pole figure of the box area in Fig.1(b), which represents the continuous evolution of the {111} poles from the undeformed state of a subsurface grain (represented by ○) to the deformed state (represented by △) after 180% plastic strain.

Using the above method, wear-induced subsurface lattice rotation were measured for 24 grains from one polycrystalline and three single crystal pins, covering a wide range of initial orientations, as shown by the {111} pole figure in Fig. 2 (a) and Table 1. During wear testing, the surface friction leads to significant shear of the subsurface grains where the rigid body rotation requires a lattice rotation around TD. Fig. 2(b) shows the rotation axis of all grains, calculated using angle/axis pair method between the initial and final orientations. It can be seen that all rotation axis cluster around TD, confirming the grains are indeed deformed by simple shear along SD. The scattering nature of rotation axis around TD is likely to originate from different slip system

activities of the individual grains. Fig. 2(c) shows the final orientations of all grains, where clustering of the grains close to ideal shear orientations such as B $\{\bar{1}12\}\langle 110\rangle$, $\bar{B}$ $\{1\bar{1}\bar{2}\}\langle\bar{1}\bar{1}0\rangle$, and A_2^* $\{11\bar{1}\}\langle 112\rangle$, can be seen. These texture components were dominant in the surface nanocrystalline layer of the same bronze after wear test under 0.5-10 kgf [24]. These observations confirm that the wear-induced subsurface lattice rotation eventually leads to the development of surface crystallographic textures, which can then affect macroscopic tribological properties such as friction coefficient and wear rate.

In addition to lattice rotation around TD, orientation spread along SD was also observed, and the spread increased at higher strain within individual grains. An example is shown in Fig.3(a) and (b) for grain G9 (as listed in Table 1), where the local misorientation angle variation is measured at various depths below the worn surface over 3.5 μm along SD. Here the misorientation angle along the profiles was measured with respect to the initial grain orientation (starting point of the arrows in Fig. 3(a). It can be seen that as strain increases from 0 to ~180%, the orientation spread increased from ~ 0.5^o to ~ 6^o over 3.5 μm. Fig.3 (c) plots the misorientation angle measured at various depths below the worn surface as a function of strain for all grains. Despite significant scattering in the data, on average, the misorientation along SD normalized by the distance of the profile along SD, θ_{SD}/d_{SD} is related to strain as $\theta_{SD}/d_{SD} = (0.57\pm0.04)\varepsilon_{vM}{}^{0.49\pm0.02}$ under sliding wear deformation. This power-law suggests that the local misorientation may be determined by the fluctuations of the dislocation distribution along SD. Interestingly it is reminiscent of power laws observed for the local slope of kinetically rough surfaces [28, 29].

Another unique data that this method provides is the continuous monitoring of lattice rotation along ND as a function of strain for individual grains. During plastic deformation, the amount of lattice rotation tend to increase with strain [15, 16]. For example, using focused hard x-ray, Margulies et al. [16] showed that the average rotation velocity is ~ 5.5° per 11% tensile deformation for pure aluminum. To date, little is known about the grain-level lattice rotation kinetics during shear, especially up to

large strain. Here, using EBSD maps, the lattice rotation along ND was investigated for all 24 grains by measuring the misorientation angle θ_{ND} at each point using two methods: (i) with respect to its neighbor as $\theta_{rel} = g_{n-1} \times {g_n}^{-1}$, where g_{n-1} and g_n are the rotation matrices of two successive grain orientations along the profile line, and (ii) with respect to the initial grain orientation as $\theta_{abs} = g_{initial} \times {g_n}^{-1}$, where $g_{initial}$ is the rotation matrix of the initial grain orientation. These measured orientation angles represent the minimum angle required to transform two orientations through a rotation angle/axis pair. For all the grains studied, θ_{rel} fluctuates between 0 and 2.5°. For the majority samples, the magnitude of this fluctuation is strain independent, as shown in Fig. 4(f) for grain G9. A few grains (e.g. grain SX1 in Fig. 4(e)) show a slight increase of this fluctuation with increasing strain. It should also be pointed out that the magnitude of θ_{rel} could be affected by the EBSD step size [30] and area size [31]. For all the grains studied, the misorientation angle θ_{abs} increases monotonically with applied strain. Among all the grains, grain G14 exhibits the highest misorientation angle of 61° while grain G18 exhibits the lowest angle of 16°. Closer observation indicates that the rate of increase of θ_{abs} as a function of strain, i.e. $\Delta\theta_{abs}/\Delta\varepsilon_{vM}$ (hereafter referred as lattice rotation rate in ND) is not a constant for any individual grain, unlike those reported for tensile deformation [16]. Two examples of the most commonly observed misorientation profiles are shown in Fig.4 (e) and (f) for grain SX1 and G9, where the lattice rotation rate increases and decreases with strain respectively. It was observed that the lattice rotation rate tends to increase with decreasing number of active slip systems (i.e. slip systems with high Schmid factor). The Schmid factor (SF) of the twelve {111}<110> slip systems for these two grains are plotted in Fig. 4 (c) and (d) as a function of distance from the worn surface, assuming simple shear deformation along SD. For grain SX1, the lattice rotation rate (i.e. the slope of the θ_{abs} vs. ε_{vM} curve) increases after the strain increases to ~ 1.2, which is reached ~ 1.82 μm below the surface according to eqn. (1). It can be seen from Fig. 4(c) that at this depth, the number of slip systems with high SF has changed. Assuming a threshold of 0.5 for 'active' slip systems (the maximum SF under simple shear is 1), the number of active slip systems of grain SX1 decreased from two, i.e. $(1\bar{1}1)[\bar{1}\bar{1}0]$ and

$(111)[0\bar{1}1]$, far away from the surface to only one (i.e. $(1\bar{1}1)[\bar{1}\bar{1}0]$) around 1.8 μm below the surface. Conversely, for grain G9 the lattice rotation rate decreases after the strain increases to ~ 0.5, which is reached ~ 5.76 μm below the surface. At this depth, the most active slip system of grain G9 changed from $(111)[\bar{1}01]$ to $(111)[\bar{1}10]$. At the same time, the number of active slip systems increased from two to three, with the addition of $(\bar{1}11)[\bar{1}\bar{1}0]$ close to the surface. Fig.4(g) summarizes θ_{rel} as a function of number of active slip systems for all grains ($n_{active\ SS}$). It can be seen that indeed, generally, θ_{rel} decreases as the number of active slip systems increases.

In summary, wear testing was used to impose a sharp strain gradient within ~ 15 μm of the surface of Cu-Ni-Sn bronze, reaching a maximum equivalent plastic strain of ≈ 181% near the surface. Using this method, the continuous evolution of local grain re-orientation as a function of deformation was directly measured using EBSD for 21 grains in a polycrystalline sample and 3 single crystal samples. Several important discoveries of this work include (1) high surface friction lead to severe shear deformation of the subsurface grains where the majority grains exhibit rotation axes around TD between the initial (at a strain of zero) and final (at a strain of ~ 181%) orientations, (2) the final orientations of all grains are close to ideal shear orientations, (3) the orientation spread along SD increases with strain following a power law relationship, and (4) the rate of lattice rotation along ND generally decreases as the number of active slip system increases. Finally, it should be pointed out that the main advantages of this approach are that large plastic strains can be reached, well exceeding those reported so far [14, 16-18], and the re-orientation measured is truly representative of a bulk behavior, since the cross-sections for EBSD analysis are prepared after the wear test, unlike the split-sample tests [14]. Furthermore, as demonstrated here, this method can be easily applied to single crystals, thus eliminating the influence of grain boundaries and neighboring grains on grain re-orientation. The material selected for the present work is a Cu-15Ni-8Sn bronze but the approach is general; for instance, preliminary results similar to those presented here have also been obtained on pure Ni. The experimental procedure detailed herein thus provides a possible avenue for direct study of grain and subgrain level plasticity in crystalline materials during severe plastic

deformation.

Acknowledgements

Stimulating discussions with Profs. A.D. Rollett, Y. Bréchet, J.-P. Chevalier, and I. Beyerlein are gratefully acknowledged. This work is supported by the National Science Foundation, Grant DMR-0906703 and DMR-1856196. Sample characterization was carried out in part in the Frederick Seitz Materials Research Laboratory Central Facilities, University of Illinois, which are partially supported by the U.S. Department of Energy under grants DE-FG02-07ER46453 and DE-FG02-07ER46471. We thank Jim Mabon for his help with orientation mapping, and Brush-Wellman for providing the bronze material used in this study.

References

[1] J.B. Singh, W. Cai, P. Bellon, Dry sliding of Cu-15 wt%Ni-8 wt%Sn bronze: Wear behaviour and micro structures, Wear 263 (2007) 830-841.

[2] W. Cai, P. Bellon, Subsurface microstructure evolution and deformation mechanism of Ag-Cu eutectic alloy after dry sliding wear, Wear 303(1-2) (2013) 602-610.

[3] T.J. Rupert, C.A. Schuh, Sliding wear of nanocrystalline Ni-W: Structural evolution and the apparent breakdown of Archard scaling, Acta Mater 58(12) (2010) 4137-4148.

[4] T.J. Rupert, W.J. Cai, C.A. Schuh, Abrasive wear response of nanocrystalline Ni-W alloys across the Hall-Petch breakdown, Wear 298 (2013) 120-126.

[5] J.F. Curry, T.F. Babuska, T.A. Furnish, P. Lu, D.P. Adams, A.B. Kustas, B.L. Nation, M.T. Dugger, M. Chandross, B.G. Clark, B.L. Boyce, C.A. Schuh, N. Argibay, Achieving Ultralow Wear with Stable Nanocrystalline Metals, Adv Mater 30(32) (2018).

[6] J.B. Singh, J.G. Wen, P. Bellon, Nanoscale characterization of the transfer layer formed during dry sliding of Cu-15 wt.% Ni-8 wt.% Sn bronze alloy, Acta Mater 56(13) (2008) 3053-3064.

[7] F. Ren, P. Bellon, R.S. Averback, Nanoscale self-organization reaction in Cu-Ag alloys subjected to dry sliding and its impact on wear resistance, Tribol Int 100 (2016) 420-429.

[8] R. Madhavan, P. Bellon, R.S. Averback, Wear Resistance of Cu/Ag Multilayers: A Microscopic Study, Acs Appl Mater Inter 10(17) (2018) 15288-15297.

[9] Y. Ohno, J. Inotani, Y. Kaneko, S. Hashimoto, Orientation Dependence of High-Angle Grain Boundary Formation during Sliding Wear in Copper Single Crystals, J Jpn I Met 74(6) (2010) 384-391.

[10] Y. Ohno, J. Inotani, Y. Kaneko, S. Hashimoto, Evolution of High-Angle Grain Boundaries in a (001) Copper Single Crystal Subjected to Sliding Wear, J Jpn I Met 73(12) (2009) 924-929.

[11] Y. Kaneko, T. Sugimoto, EBSD Analysis of Microstructure Evolution of Pure Iron Subjected to Sliding Wear and Related Change in Vickers Microhardness, Mater Trans 55(1) (2014) 85-92.

[12] S.C. Gallo, H.S. Dong, EBSD and AFM observations of the microstructural changes induced by low temperature plasma carburising on AISI 316, Appl Surf Sci 258(1) (2011) 608-613.

[13] A.V. Chumaevskii, S.Y. Tarasov, D.V. Lychagin, Plastic Strain Arrangement in Copper Single Crystals in Sliding, Aip Conf Proc 1623 (2014) 91-94.
[14] S. Panchanadeeswaran, R.D. Doherty, R. Becker, Direct observation of orientation change by channel die compression of polycrystalline aluminum - Use of a split sample, Acta Mater 44(3) (1996) 1233-1262.
[15] L. Zhu, M. Seefeldt, B. Verlinden, Deformation banding in a Nb polycrystal deformed by successive compression tests, Acta Mater 60(10) (2012) 4349-4358.
[16] L. Margulies, G. Winther, H.F. Poulsen, In situ measurement of grain rotation during deformation of polycrystals, Science 291(5512) (2001) 2392-2394.
[17] J.S. Zhang, S.J. Hao, D.Q. Jiang, Y. Huan, L.S. Cui, Y.O. Liu, H. Yang, Y. Ren, In situ synchrotron high-energy X-ray diffraction study of microscopic deformation behavior of a hard-soft dual phase composite containing phase transforming matrix, Acta Mater 130 (2017) 297-309.
[18] S.F. Nielsen, H.F. Poulsen, F. Beckmann, C. Thorning, J.A. Wert, Measurements of plastic displacement gradient components in three dimensions using marker particles and synchrotron X-ray absorption microtomography, Acta Mater 51(8) (2003) 2407-2415.
[19] B. Barzdajn, A.T. Paxton, D. Stewart, F.P.E. Dunne, A crystal plasticity assessment of normally-loaded sliding contact in rough surfaces and galling, J Mech Phys Solids 121 (2018) 517-542.
[20] I.J. Beyerlein, L.S. Toth, Texture evolution in equal-channel angular extrusion, Prog Mater Sci 54(4) (2009) 427-510.
[21] Y. Estrin, A. Molotnikov, C.H.J. Davies, R. Lapovok, Strain gradient plasticity modelling of high-pressure torsion, J Mech Phys Solids 56(4) (2008) 1186-1202.
[22] H.Z. Yu, M.E. Jones, G.W. Brady, R.J. Griffiths, D. Garcia, H.A. Rauch, C.D. Cox, N. Hardwick, Non-beam-based metal additive manufacturing enabled by additive friction stir deposition, Scripta Mater 153 (2018) 122-130.
[23] Supplementary material.
[24] W. Cai, J. Mabon, P. Bellon, Crystallographic textures and texture transitions induced by sliding wear in bronze and nickel, Wear 267(1-4) (2009) 485-494.
[25] W. Cai, P. Bellon, Microstructural self-organization triggered by twin boundaries during dry sliding wear, Acta Mater 60(19) (2012) 6673-6684.
[26] D.A. Rigney, M.G.S. Naylor, R. Divakar, L.K. Ives, Low-Energy Dislocation-Structures Caused by Sliding and by Particle Impact, Materials Science and Engineering 81(1-2) (1986) 409-425.
[27] S. Kailas, J Mat Eng Perf 12 (2003) 629-637.
[28] J.M. Lopez, M. Castro, R. Gallego, Scaling of local slopes, conservation laws, and anomalous roughening in surface growth, Phys Rev Lett 94(16) (2005).
[29] J. Krug, Kinetic pattern formation at solid surfaces, Collective Dynamics of Nonlinear and Disordered Systems (2005) 5-37.
[30] P.J. Konijnenberg, S. Zaefferer, D. Raabe, Assessment of geometrically necessary dislocation levels derived by 3D EBSD, Acta Mater 99 (2015) 402-414.
[31] P.O. Guglielmi, M. Ziehmer, E.T. Lilleodden, On a novel strain indicator based on uncorrelated misorientation angles for correlating dislocation density to local strength, Acta Mater 150 (2018) 195-205.

Table 1. Summary of the initial orientations (local grain orientation far away from the wear surface) of 24 individual grains investigated. G1-G21 are measured from a polycrystalline bronze pin and SX1-SX3 are measured from three single crystal bronze pins.

Grain ID	Bunge-Euler angles (ϕ_1 ϕ ϕ_2)(degree)		
G1	70.8	43.3	31.4
G2	160.2	21.3	4.3
G3	163.1	27.5	7.7
G4	314.8	40.5	55.2
G5	117.7	8.2	67.9
G6	239.8	22.1	67.1
G7	240.0	17.6	80.5
G8	25.6	30.5	60.3
G9	318.8	32.5	49.4
G10	5.50	42.8	88.5
G11	221.0	17.8	18.0
G12	105.9	49.4	46.8
G13	337.7	20.9	15.6
G14	73.7	42.6	0.2
G15	358.4	18.0	13.8
G16	344.5	24.7	25.1
G17	164.4	52.2	46.0
G18	44.6	31.7	33.0
G19	269.8	32.8	10.4
G20	38.2	42.9	66.0
G21	324.7	27.7	81.6
SX1	221.5	27.2	88.0
SX2	342.2	30.2	18.8
SX3	286.0	38.4	50.3

Figure Captions

Figure 1. (a) Schematic illustration of the pin-on-disc (POD) wear test. SD, TD, and ND represent the sliding, transverse, and normal directions respectively. (b) Cross-section orientation map from subsurface grain with orientation in ND direction. The orientation map is colored coded according to the triangle legend at the bottom. (c) Effective strain as a function of distance from the sliding surface obtained by marker displacement technique. (d) {111} pole figure of the box area in (b) using equal area projection, where ○ and △ represent respectively the initial ($\varepsilon_{vM} = 0$) and final ($\varepsilon_{vM} = 181\%$) orientation of the subsurface grain. (e) Bright-field TEM image of cross-section of the bronze pin after wear test. Dashed line indicates the wear surface.

Figure 2. (a) {111} pole figures of measured initial ($\varepsilon_{vM} = 0$) orientations, (b) rotation axis measured by final to initial orientation, and (c) final ($\varepsilon_{vM} = 181\%$) orientations of 24 grains from polycrystalline and single crystalline bronze pins.

Figure 3. (a) Cross-section orientation map from subsurface grain G9 with orientation in ND direction. (b) Misorientation angle (in degrees) at various depths below the worn surface, as marked in (a). (c) Summary of misorientation angles as a function of von Mises strain for all grains (with an arbitrary color assigned to each grain). The orientation map in (a) is colored coded according to the triangle legend in Fig. 1(b).

Figure 4. Cross-section orientation map (with orientation in ND direction) of grain (a) SX1 and (b) G9 (as listed in Table 1). (c) and (d) The corresponding Schmid factor profiles as a function of distance from the surface. (e) and (f) The corresponding relative and absolute misorientation as a function of strain. (g) Summary of relative misorientation as a function of number of active slip systems for all grains. The relative misorientations are measured between two consecutive data points along the profile while the absolute misorientations are measured with respect to the initial grain orientation. The orientation maps in (a) and (b) are colored coded according to the

triangle legend in Fig. 1(b). An arbitrary color is assigned to each grain in (g).

Supplementary Material

Click here to download Supplementary Material: Supplemental material.pdf

*Graphical Abstract

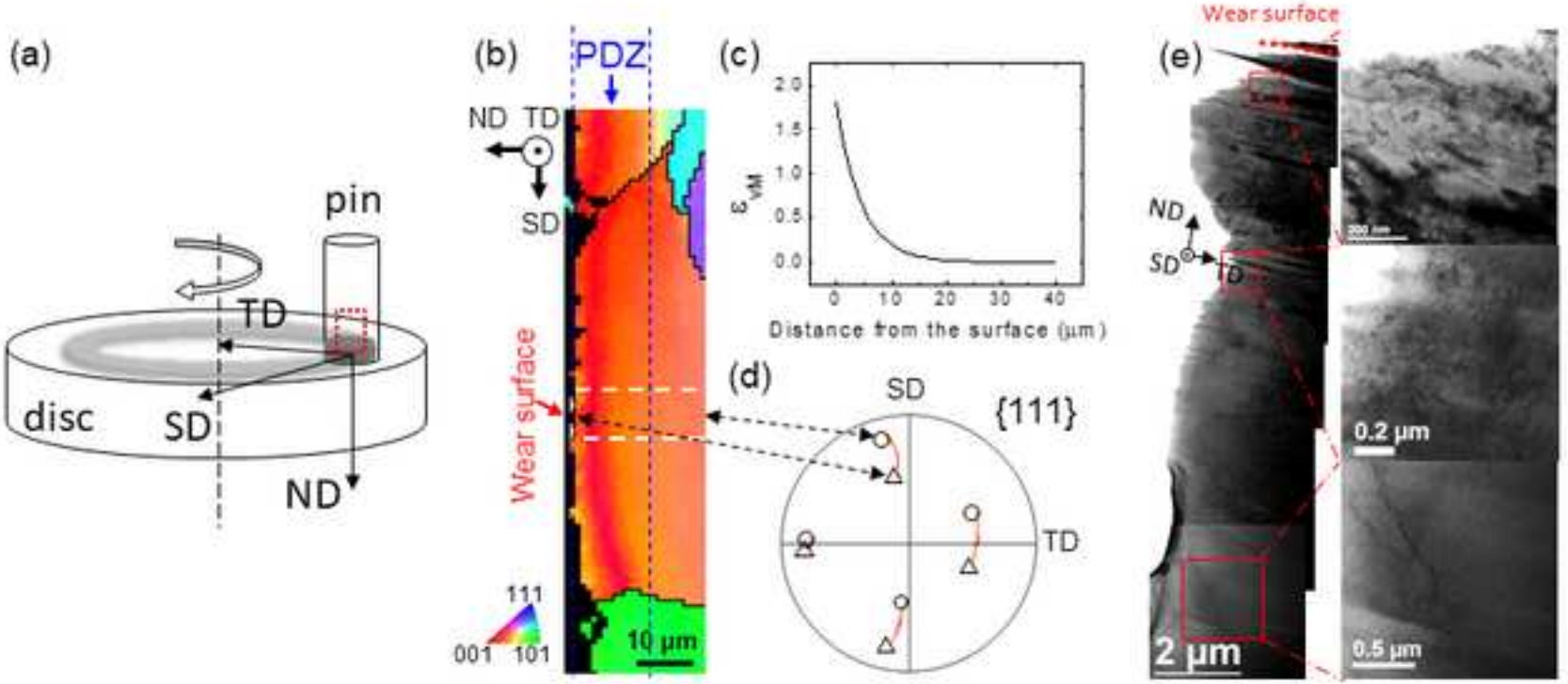

Figure 1
Click here to download high resolution image

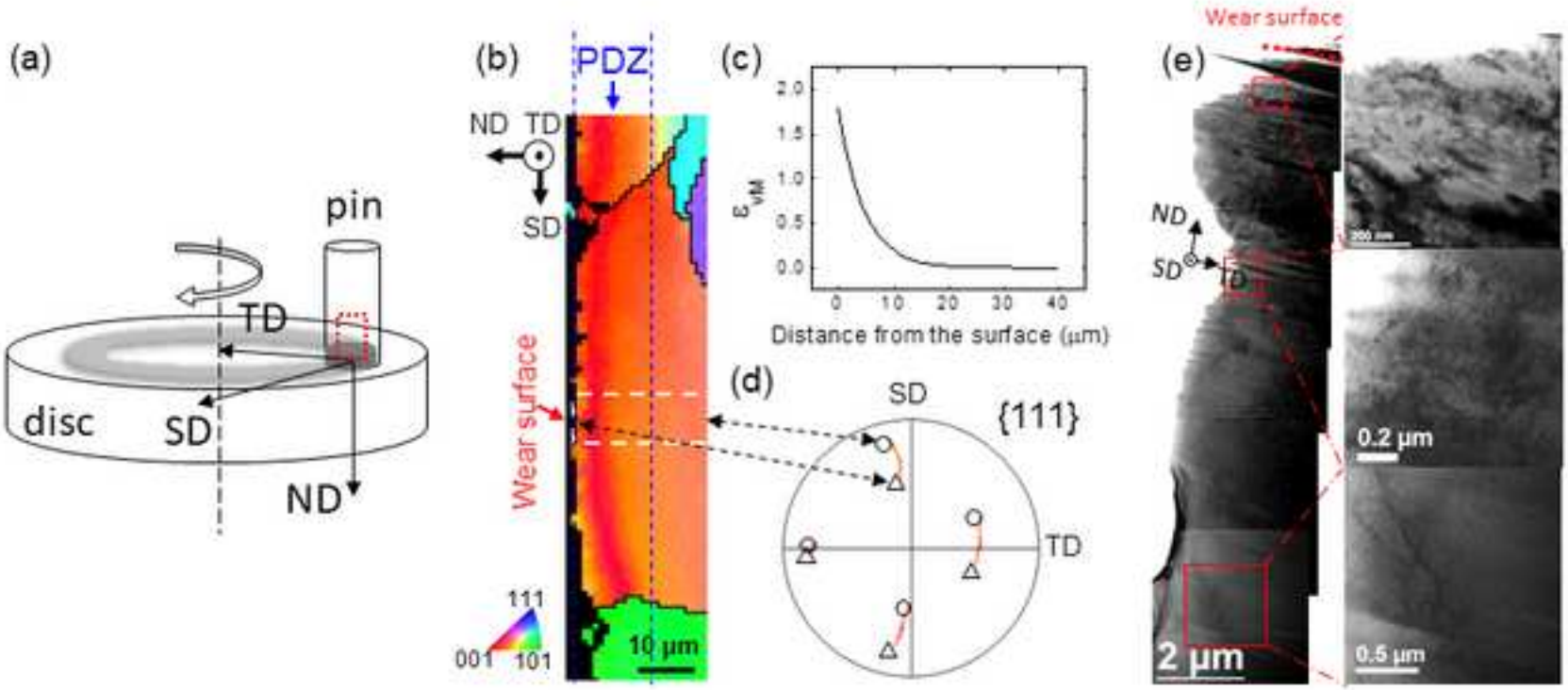

Figure 1. (a) Schematic illustration of the pin-on-disc (POD) wear test. SD, TD, and ND represent the sliding, transverse, and normal directions respectively. (b) Cross-section orientation map from subsurface grain with orientation in ND direction. The orientation map is colored coded according to the triangle legend at the bottom. (c) Effective strain as a function of distance from the sliding surface obtained by marker displacement technique. (d) {111} pole figure of the box area in (b) using equal area projection, where ○ and △ represent respectively the initial ($\varepsilon_{vM} = 0$) and final ($\varepsilon_{vM} = 180\%$) orientation of the subsurface grain. (e) Bright-field TEM image of cross-section of the bronze pin after wear test. Dashed line indicates the wear surface.

Figure 2
Click here to download high resolution image

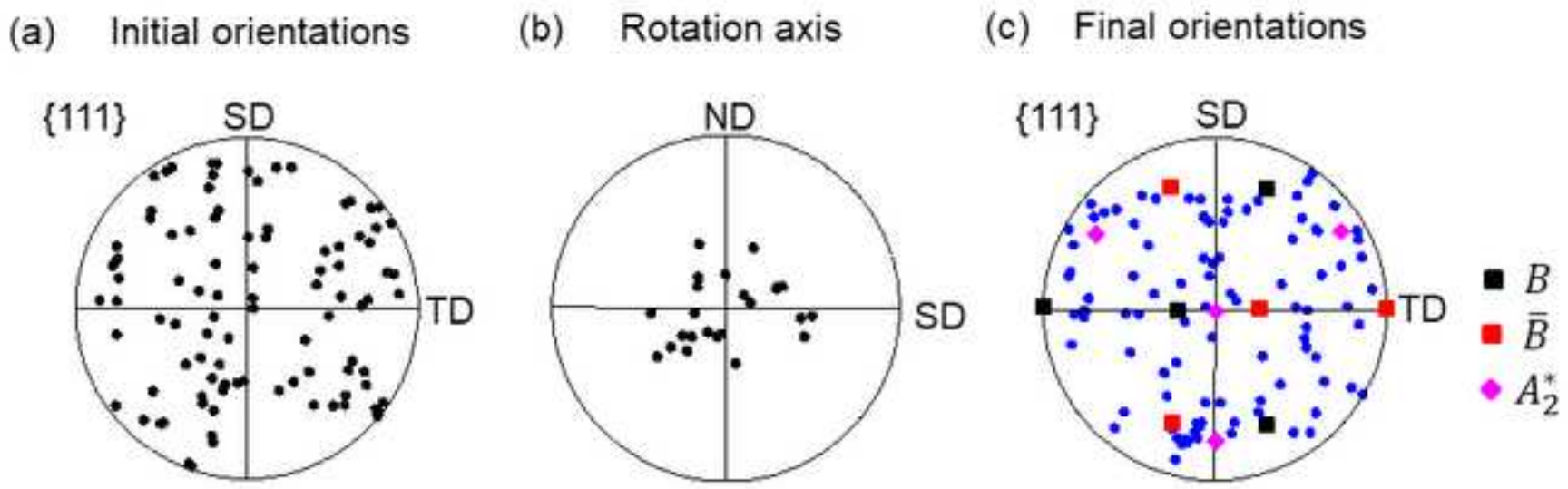

Figure 2. (a) {111} pole figures of measured initial ($\varepsilon_{vM} = 0$) orientations, (b) rotation axis measured by final to initial orientation, and (c) final ($\varepsilon_{vM} = 180\%$) orientations of 24 grains from polycrystalline and single crystalline bronze pins.

Figure3
Click here to download high resolution image

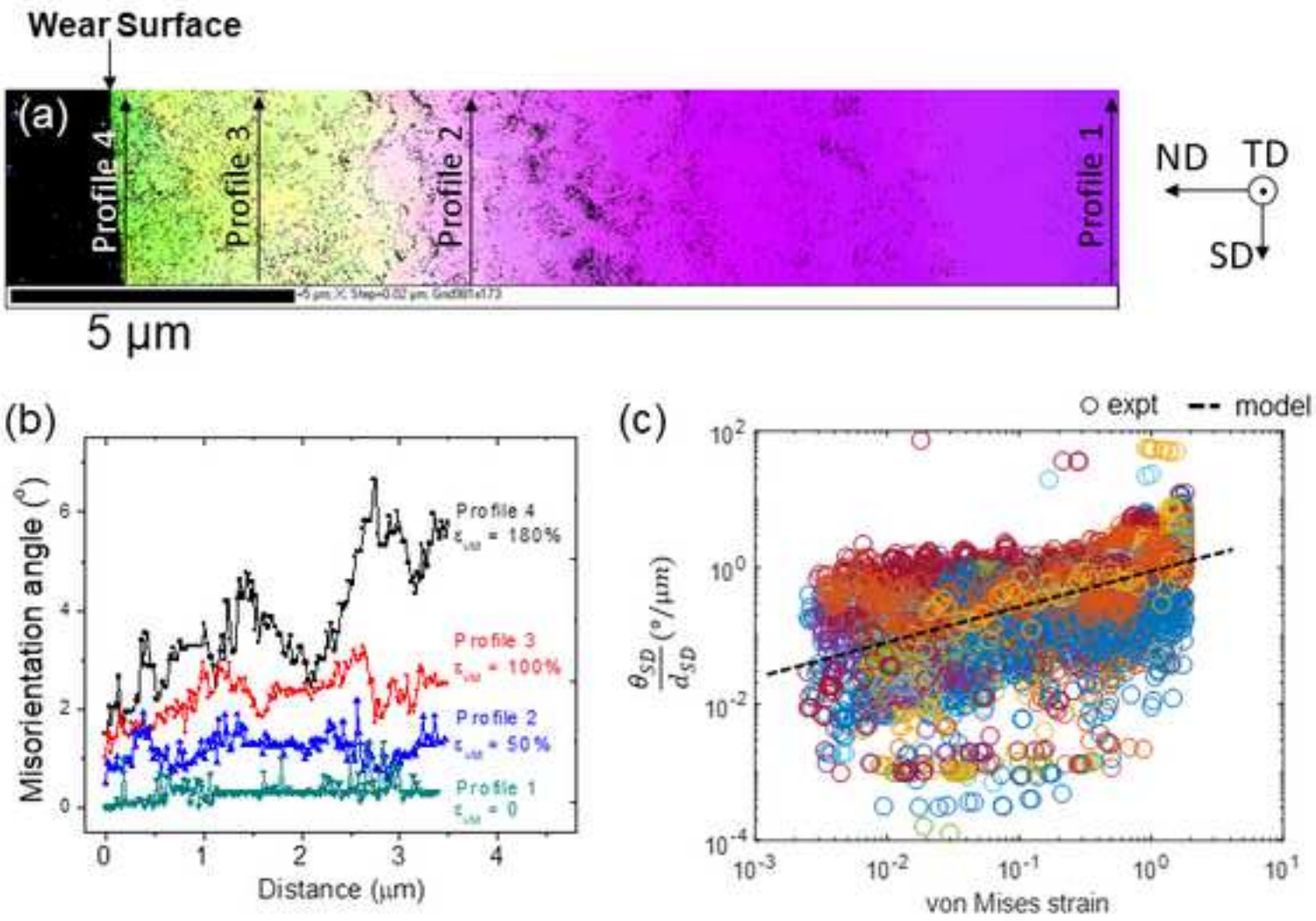

Figure 3. (a) Cross-section orientation map from subsurface grain G9 with orientation in ND direction. (b) Misorientation angle (in degrees) at various depths below the worn surface, as marked in (a). (c) Summary of misorientation angles as a function of von Mises strain for all grains (with an arbitrary color assigned to each grain). The orientation map in (a) is colored coded according to the triangle legend in Fig. 1(b).

Figure4
Click here to download high resolution image

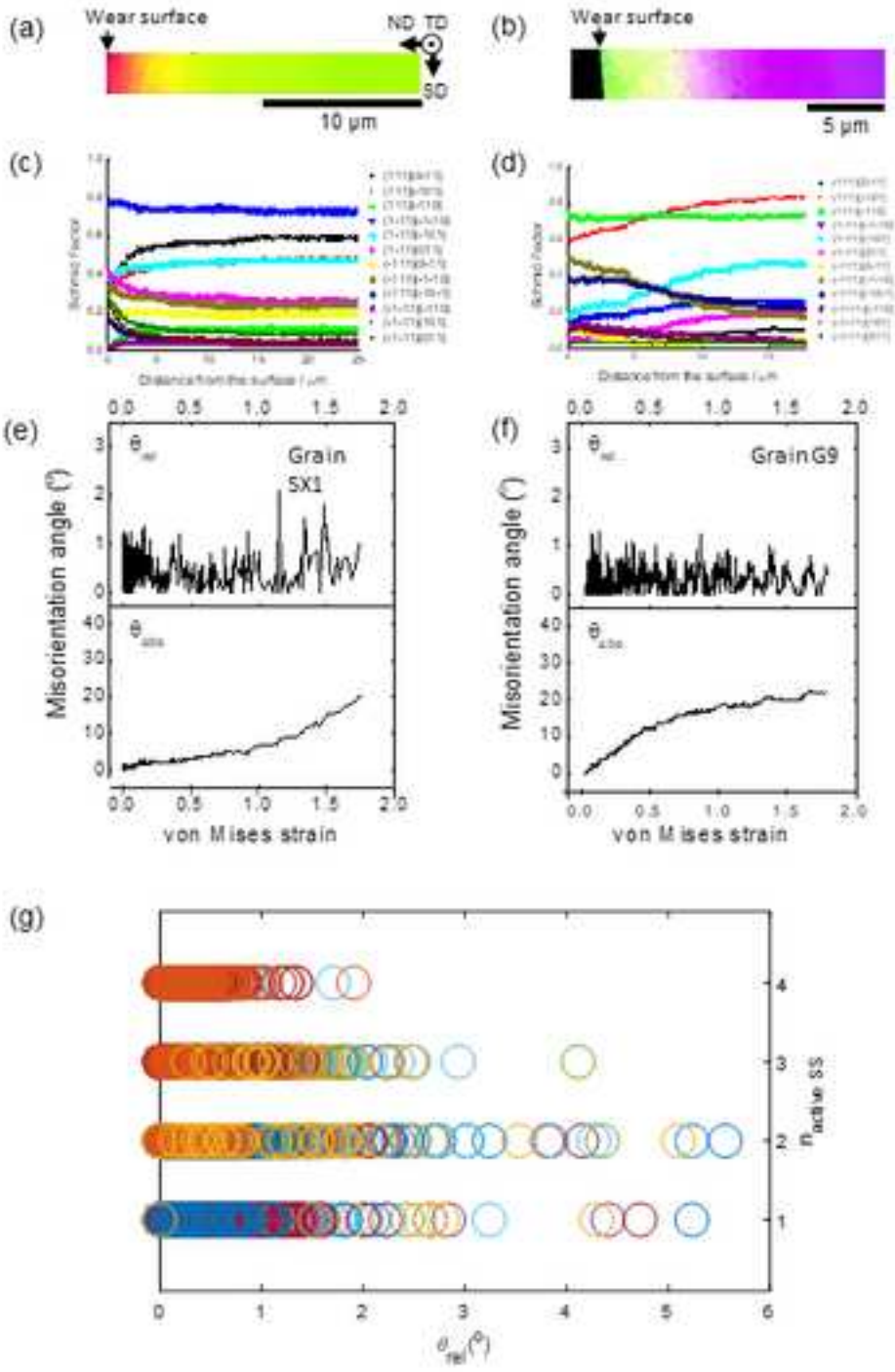

Figure 4. Cross-section orientation map (with orientation in ND direction) of grain (a) SX1 and (b) G9 (as listed in Table 1). (c) and (d) The corresponding Schmid factor profiles as a function of distance from the surface. (e) and (f) The corresponding relative and absolute misorientation as a function of strain. (g) Summary of relative misorientation as a function of number of active slip systems for all grains. The relative misorientations are measured between two consecutive data points along the profile while the absolute misorientations are measured with respect to the initial grain orientation. The orientation maps in (a) and (b) are colored coded according to the triangle legend in Fig. 1(b). An arbitrary color is assigned to each grain in (g).